Title

Thermoelectric performance and the role of anti-site disorder in the 24-electron Heusler $TiFe_2Sn$

Journal

Journal of Physics: Condensed Matter, 29(40)

ISSN

0953-8984 1361-648X

Authors

Buffon, Malinda L C
Laurita, Geneva
Lamontagne, Leo
et al.

Publication Date

2017-10-11

DOI

10.1088/1361-648X/aa81e7

Peer reviewed

Thermoelectric performance and the role of anti-site disorder in the 24-electron Heusler $TiFe_2Sn$

Malinda L. C. Buffon,[1,2] **Geneva Laurita,**[2] **Leo Lamontagne,**[1,2] **Emily E. Levin,**[1,2] **Shahryar Mooraj,**[2,3] **Demetrious L. Lloyd,**[2,4] **Natalie White,**[5] **Tresa M. Pollock,**[1,2] **and Ram Seshadri**[1,2,4]

[1] Materials Department, University of California, Santa Barbara, CA 93106
[2] Materials Research Laboratory, University of California, Santa Barbara, CA 93106
[3] Department of Physics, University of California, Santa Barbara, CA 93106
[4] Department of Chemistry and Biochemistry, University of California, Santa Barbara, CA 93106
[5] Department of Chemistry and Biochemistry, Jackson State University, Jackson, MS 39217

E-mail: mandibuffon@mrl.ucsb.edu

Abstract. Heusler compounds XY_2Z with 24 valence electrons per formula unit are potential thermoelectric materials, given their thermal and chemical stability and their relatively earth-abundant constituent elements. First principal calculations on this compound suggest semiconducting behavior of $TiFe_2Sn$, and a relatively flat conduction band that could be associated with a high Seebeck coefficient upon electron doping. $TiFe_2Sn$ as a thermoelectric material has been studied via synchrotron X-ray and neutron diffraction studies that characterize site order/disorder phenomena. Samples fabricated by a three step processing approach were subjected to high temperature Seebeck and electrical resistivity measurements. Ti:Fe anti-site disorder is present in the stoichiometric compound and these defects are reduced in Ti–rich compositions. Additionally, we investigate control of the Seebeck coefficient through the introduction of carriers through the substitution of Sb on the Sn site in these intrinsically p-type materials.

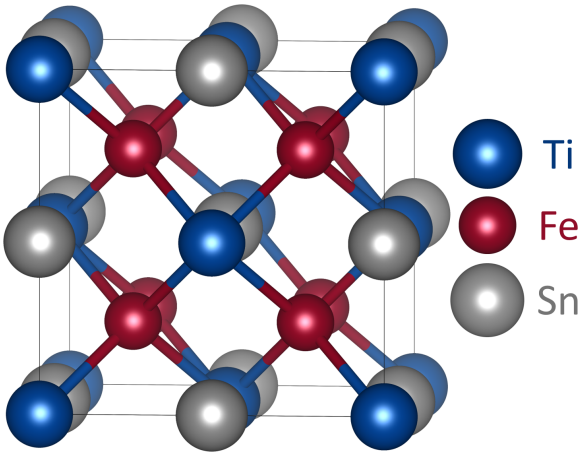

Figure 1. Representation of the cubic XY_2Z Heusler $TiFe_2Sn$ in space group $Fm\bar{3}m$. The blue X Ti occupy the 4a $(0,0,0)$ Wyckoff sites, red Y Fe atoms occupy 8c $(\frac{1}{4},\frac{1}{4},\frac{1}{4})$, and grey Z Sn atoms occupy $4b$ $(\frac{1}{2},\frac{1}{2},\frac{1}{2})$.

Introduction

Thermoelectric devices, through their clean conversion of waste heat into energy, are of substantial interest to the future of sustainable energy. The desirable performance metric in these materials is described by the thermoelectric figure of merit, $zT = [S^2/(\kappa\rho)]T$, where S is the Seebeck coefficient, κ is the thermal conductivity, and ρ is the electrical resistivity of the material at a given temperature T.[1] A vast number of materials and material classes, exemplified by Bi_2Te_3,[2] clathrates,[3], skutterudites,[4] have been explored to optimize thermoelectric properties. Heusler and half-Heusler materials are of particular interest for moderate temperature ($800 < \mathrm{T} < 1073$ K) thermoelectric applications, such as recapturing waste heat from automobile exhaust, due to the large Seebeck coefficients displayed by some of them ($|S| > 200\,\mu$V/K) as well as mechanical, thermal, and chemical stability at operating temperatures.[5]

The class of compounds discussed here were discovered in 1903 when Heusler found that $MnCu_2Sn$ is magnetic despite containing no magnetic elements.[6] Figure 1 illustrates the Heusler crystal structure, which can be viewed as four interpenetrating face-centered cubic sublattices. Heusler compounds have the chemical formula XY_2Z, where X and Y are generally transition metals and Z is a main group element. These compounds are expected to be semiconducting when the total valence electron count (VEC) is 24.[7] The 24 VEC Heusler compounds such as $TiFe_2Sn$ and VFe_2Al are of potential value as thermoelectrics due to relatively small band gaps. Anti-site disorder[8] and other structural defects[9] are characteristic to Heusler compounds, influencing the band structure[10] and electrical properties including the resistivity and Seebeck coefficient.

Recent computational investigation on the Heusler compound $TiFe_2Sn$ have pointed to the ability to enhance the Seebeck coefficient of this compound through

n-type doping.[11] These predictions are aligned with what is known for the well-studied Heusler compound VFe_2Al that has been of interest since the discovery of unusual temperature dependence of electrical resistivity[12] attributed to a pseudogap at the Fermi level.[13, 14] VFe_2Al displays a large Seebeck coefficient ($|S| > 150\,\mu$V/K) upon varying the VEC slightly from 24, achieved by introducing Ge[15] or Si[16] to the Al site, varying the V–Al ratio,[17, 18, 19] and varying the Fe–V ratio.[20, 21] In contrast to VFe_2Al, $TiFe_2Sn$ is a less explored compound, and the existing literature on $TiFe_2Sn$ has not indicated significant improvements in Seebeck coefficient upon varying the Ti:Fe ratio.[22, 23] This discrepancy between calculations and experimental results is likely the result of anti-site Ti/Fe disorder, as has been suggested by lab X-ray diffraction and Mössbauer studies.[24, 25, 26] The anti-site disorder takes on the form of Ti occupying Fe sites (Ti_{Fe}) and as Fe occupation on Ti sites (Fe_{Ti}).

Here we employ synchrotron X-ray and neutron diffraction studies to understand the structure and composition, including anti-site disorder, in $TiFe_2Sn$. We have used two different approaches to probe the role of disorder and charge carrier doping in $TiFe_2Sn$. First, the Ti:Fe ratio was varied using small changes in the starting values of x in the preparation of $Ti_{1+x}Fe_{2-x}Sn$ to examine the impact this ratio has on anti-site disorder. Second, the effect of Sb for Sn in $TiFe_2Sn_{1-y}Sb_y$ was explored to understand trends in the thermoelectric performance, examining predictions that a high Seebeck in $TiFe_2Sn$ will manifest with n-type doping.[11] We find that anti-site disorder critically impacts properties in these materials, and indeed, $TiFe_2Sn$ fails to display true semiconductor behavior. While the addition of extra charge carriers through Sb substitution does impact the Seebeck coefficient, the result is eventually detrimental to properties since holes of the intrinsically p-type parent materials are compensated by the doped electrons.

Methods

Electronic structure calculations of $TiFe_2Sn$ were carried out using density functional theory (DFT) as implemented in the Vienna ab initio Simulation package (VASP),[27, 28] using projector-augmented wave (PAW) pseudopotentials.[29, 30] The Perdew-Burke-Ernzerhof (PBE) exchange correlation functional was employed for the calculations,[31] with a Γ-centered k-mesh of $8 \times 8 \times 8$.

Two series of compounds based on $TiFe_2Sn$ were prepared. One set of compounds varied the Ti:Fe ratio according to $Ti_{1+x}Fe_{2-x}Sn$ ($x = -0.10$, -0.05, 0, 0.05, 0.10) to examine how off-stoichiometry impacts site ordering and thermoelectric properties. A second set of compounds were prepared by substituting the Sn site with Sb according to $TiFe_2Sn_{1-y}Sb_y$ ($y = 0.01$, 0.05) to explore the suggestion that the Seebeck coefficient can be enhanced with n-type doping.[11]

All samples were prepared using a three step processing method: arc-melting, annealing, and spark plasma sintering (SPS). Arc-melting was carried out in an inert

Ar atmosphere from appropriate stoichiometric ratios of the pure elements: Ti foil (99.7%, Sigma Aldrich), Fe chips (99.98%, Sigma Aldrich), Sn shot (99.8%, Sigma Aldrich), and Sb shot (99.999%, Alfa Aesar). The resulting button was wrapped in Ta foil, sealed in a silica ampoule under a partial pressure of Ar, and annealed for one week at 1123 K from which the furnace was turned off and allowed to return to room temperature. Following the anneal, the button was ground to a fine powder using a mortar and pestle. This powder was compacted in a graphite die in the SPS system (FCT Systeme GmbH, Germany) for 8 min. at 61.5 MPa and 1123 K to produce a puck approximately 9.1 mm in diameter. Final samples were roughly 1.5 g in mass. Bars for physical property measurements of approximate dimensions $6 \times 2 \times 3$ mm were sectioned by electrical discharge machining. Remaining sections were preserved for electron microscopy analysis.

Powder samples for $x = -0.10$, -0.05, 0, 0.05, 0.10 and $y = 0.01$, 0.05 were sealed in Kapton capillary tubes and synchrotron X-ray diffraction (XRD) data was acquired at 295 K for all samples on the 11-BM beamline at the Advanced Photon Source at Argonne National Laboratory with a wavelength of 0.4593 Å, selected in order to avoid absorption by Sn. Neutron diffraction data for $x = -0.10$, 0, 0.10 and $y = 0.05$ was acquired by the POWGEN diffractometer at the Spallation Neutron Source located at Oak Ridge National Laboratory. Samples were loaded in 6 mm vanadium cans and measurements were carried out at 300 K, lasting approximately 1 h. Rietveld refinements of diffraction data was performed using the TOPAS software suite.[32] When possible (for $x = -0.10$, 0.00, 0.10 and $y = 0.05$) joint X-ray and neutron refinements were carried out. The $TiFe_2Sn$ crystal structure was visualized using VESTA.[33]

Samples for scanning electron microscopy analysis were sectioned from final SPS pucks, mounted in epoxy, ground with SiC paper, and then polished with diamond suspensions down to 0.25 μm. Scanning electron microscopy (SEM) was carried out on a FEI XL30 Sirion FEG equipped with a backscattered electron (BSE) detector operating at 15.0 kV. Phase identification was supported by energy dispersive X-ray (EDX) analysis.

High temperature electrical transport properties (Seebeck coefficient, S, and electrical resistivity, ρ) were measured using an ULVAC ZEM-3 instrument. Measurements were carried out under 0.1 atm of He and consisted of heating the sample from 300 K to 850 K and cooling to 300 K. Measurements were taken at 50 K intervals and results collected on cooling are presented.

Results and Discussion

Band Structure Computations

First-principal DFT calculations of the electronic band structure of $TiFe_2Sn$, shown in Figure 2, indicate that $TiFe_2Sn$ is a semiconductor with an indirect band gap of 0.1 eV.

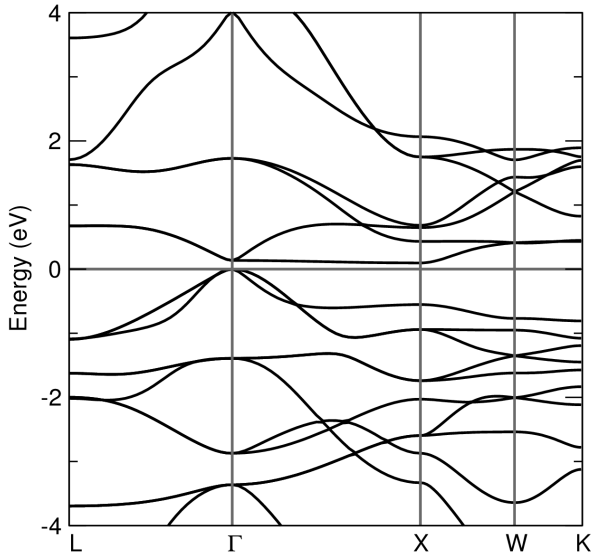

Figure 2. PBE electronic band structure of Heusler compound $TiFe_2Sn$. Calculations indicate the indirect band gap between X and Γ is 0.1 eV while the direct gap at Γ is 0.14 eV. The low curvature conduction band between Γ and X implies a large Seebeck coefficient is attainable with n-type doping.

The electronic band structure reveals a flat conduction band that rises only 0.04 eV between the conduction band minimum at X and nearby Γ. As the Seebeck coefficient is proportional to the effective mass,[1] a large Seebeck coefficient is expected with n-type doping. Yabuuchi *et al.*[11] reports a band gap of 0.07 eV and estimates that a high Seebeck coefficient ($S < -200\,\mu$V/K) would manifest upon n-type doping, on the order of 10^{21} cm^{-3}. This band structure is consistent with published band structure calculations[34, 35, 36] that also evaluate the density of state (DOS), indicating that the conduction band is primarily comprised of Fe states.

Structural Characterization

In order to examine site ordering in $TiFe_2Sn$, we carried out detailed synchrotron X-ray and neutron diffraction studies on material with stoichiometric deviations from $TiFe_2Sn$. Synchrotron X-ray diffraction, due to its Q-space resolution and high signal to noise ratio, allows for accurate determination of lattice parameters and identification of minor impurity phases. Neutron diffraction also enables the determination of accurate site occupancies and atomic displacement parameters, reported as U_{iso} (Å^2).

Representative Rietveld fits of the neutron and synchrotron X-ray diffraction patterns for $x = 0$ are shown in Figure 3. Rietveld refinements were performed for X-ray data for the $x = -0.05$, 0.05 samples and both X-ray and neutron diffraction data for $x = -0.10$, 0, 0.10. The quality of fit metric, R_{wp}, was in the range of 7 to 10% for all refinements. Impurity phases were determined by evaluating minor peaks of X-ray data. Compounds with compositions near $TiFe_2Sn$ ($x = -0.05$, 0, 0.05) did not form

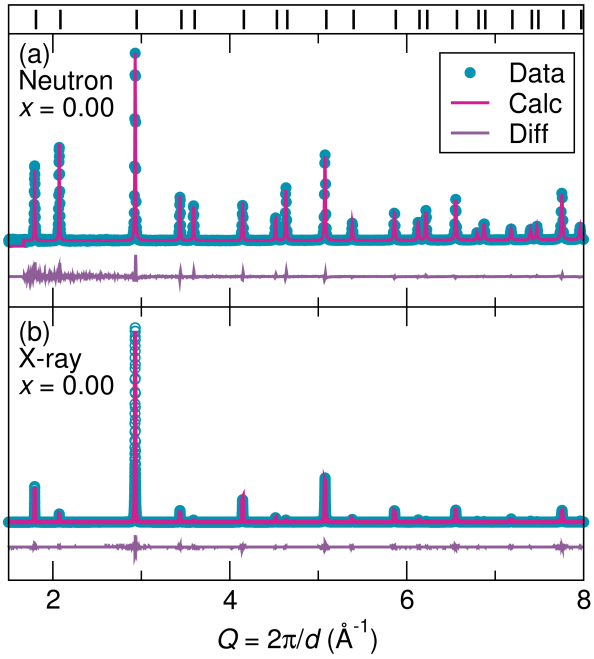

Figure 3. Joint fits of (a) neutron and (b) synchrotron X-ray diffraction data for stoichiometric $TiFe_2Sn$. Indexed peaks from the refined Heusler phase is shown in the top panel, corresponding with diffraction results. Difference curves are plotted below each fit.

any detectable impurity phases. The Fe–rich sample ($x = -0.10$) contained 0.3 wt% elemental Sn impurities, while analysis of the Ti–rich sample ($x = 0.10$) shows the formation of 0.4 wt% Sn_5Ti_6. The formation of impurity phases at extremes indicates that this study evaluates the full solubility limit across the investigated Ti:Fe ratio. A subtle peak asymmetry is present in X-ray peaks, possibly suggesting a distribution of lattice parameters, as has been suggested elsewhere.[26, 25] However, fitting this asymmetry with an additional $TiFe_2Sn$ phase did not visually improve the fit or R_{wp}.

Structural parameters, as determined by Rietveld refinements, are presented in Figure 4. We determined a lattice parameter of 6.06304(1) Å for pure $TiFe_2Sn$ which is in agreement with previous studies.[26, 11] Panel (a) of Figure 4 presents variations in the lattice parameter of $TiFe_2Sn$ with x, illustrating that while excess Fe ($x < 0$) either expands or slightly contracts the lattice parameter, excess Ti ($x > 0$) results in a clearly contracted lattice. This result is consistent with site occupancy results illustrated in panel (b) and anti-site occupancy results shown in panel (c) of Figure 4. To allow the accurate determination of Ti_{Fe} and Fe_{Ti} anti-site defects, refinements were completed by constraining each atomic site to be filled (*i.e.* no vacancies) while allowing the site to contain both Ti or Fe atoms. The Sn occupancy was fixed to full site occupancy to reduce correlation effects. While other defect arrangements were evaluated, this methodology resulted in the best fit and the least amount of correlation between the refined parameters. The refinement of atomic displacement parameters resulted in U_{iso} values of 0.002 Å to 0.006 Å, clarifying that structural

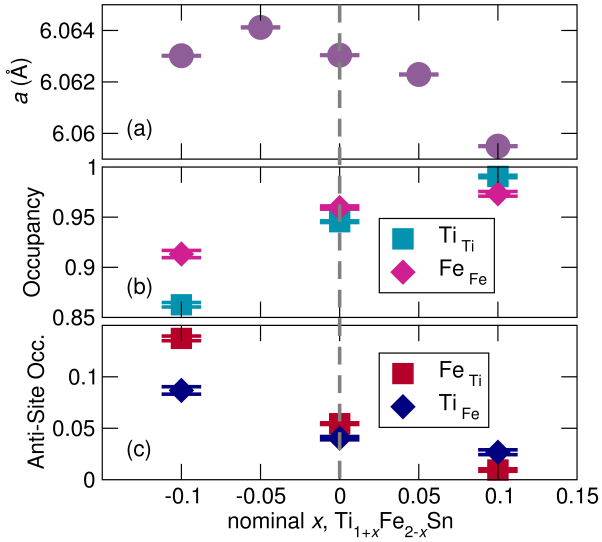

Figure 4. Summary of $Ti_{1+x}Fe_{2-x}Sn$ structural parameters: (a) lattice parameter (b) site occupancy (c) anti-site occupancy, illustrating that the $x = 0$ composition has Ti/Fe anti-site disorder that can be reduced by using a Ti–rich composition. Data was obtained from Rietveld refinement of diffraction data ($x = -0.05$, 0.05) and joint refinement of X-ray and neutron diffraction data ($x = -0.10$, 0, 0.10). Error bars are shown.

disorder (*i.e.* atoms disordered about their ideal site) does not play a large role in these compounds. These occupancy results suggest that anti-site defects are present in all samples. However, the quantity of these defects is considerably reduced for the Ti–rich, $x = 0.10$, compound. This is consistent with the contraction in lattice parameter for this compound.

In addition to evaluating the effect of varying the Ti:Fe ratio in $TiFe_2Sn$, n-type doping of $TiFe_2Sn$ was attempted by the substitution of Sb onto the Sn site by preparing samples with composition $TiFe_2Sn_{1-y}Sb_y$ ($y = 0.01$, 0.05). Neutron and X-ray diffraction of $TiFe_2Sn_{0.95}Sb_{0.05}$ is presented in panels (a) and (b), respectively, of Figure 5. No impurity phases were identified in these compounds. To reduce correlation effects, Rietveld refinements were performed with Ti and Fe anti-site defects fixed to the values in Figure 4. Noting that these elements have similar X-ray and coherent neutron scattering lengths (the latter are 6.225 fm for Sn and 5.57 fm for Sb [37]) occupancy refinements did not yield physically meaningful results, suggesting that refinement of site occupancies is not effective for this material. However, lattice parameters, displayed in Figure 5(c) with respect to y, decrease as y increases. To evaluate this decrease, a linear Vegard law expression[38] was calculated, utilizing a theoretical lattice parameter of Heusler $TiFe_2Sb$.[35] This line approximates the lattice constants shown in Panel (c) of Figure 5, indicating that the lattice contracts with Sb introduction, as expected, suggesting the substitution of Sb atoms onto the Sn site.

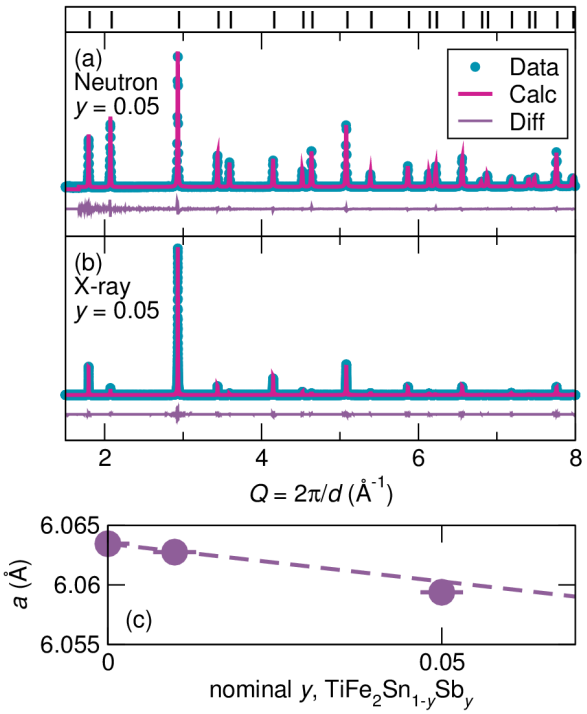

Figure 5. Joint refinement fits of (a) neutron and (b) X-ray diffraction data for $TiFe_2Sn_{0.95}Sb_{0.05}$. Panel (c) indicates that the lattice parameter of $TiFe_2Sn_{1-y}Sb_y$ generally decreases with y, relating to a Vegard's law estimation of lattice parameter, indicated by the dashed line.

Microscopy

Microstructural analysis was performed for these materials utilizing SEM with a BSE detector to highlight Z contrast. EDX was used to examine elemental ratios, characterize matrix phase compositional changes, and resolve impurity phases. Representative micrographs were taken for a subset of samples ($x = -0.10$, 0.00, 0.10) as displayed in Figure 6. EDX measurements indicate that the matrix phase of $Ti_{0.9}Fe_{2.1}Sn$ ($x = -0.10$) is Fe–rich, while the atomic ratio of the matrix phase of $Ti_{1.1}Fe_{1.9}Sn$ ($x = 0.10$) is Ti–rich. EDX was also employed to enable the identification of impurity phases that, according to X-ray diffraction, make up less than 1 wt % of these samples. For all samples, impurity phases form near grain boundaries. In $Ti_{0.9}Fe_{2.1}Sn$ ($x = -0.1$) $FeSn_2$ was determined as the impurity phase, identifiable by its bright appearance in Figure 6 (a). This result differs from analysis of X-ray diffraction, which indicated Sn as the primary impurity phase. This discrepancy may result from inadvertent sampling surrounding material. For the pure compound, ($x = 0$, Figure 6 (b)) a Ti–rich impurity phase can be seen as dark diamond-shaped regions residing between grains and is present only in trace amounts, in agreement with XRD refinements which indicates no extra phases. Evaluation of $Ti_{1.1}Fe_{1.9}Sn$, ($x = 0.1$) shown in panel (c) indicates that Sn_5Ti_6 with excess Fe solubility is the impurity phase which, upon allowing lattice expansion for Fe inclusion, agrees with our X-ray

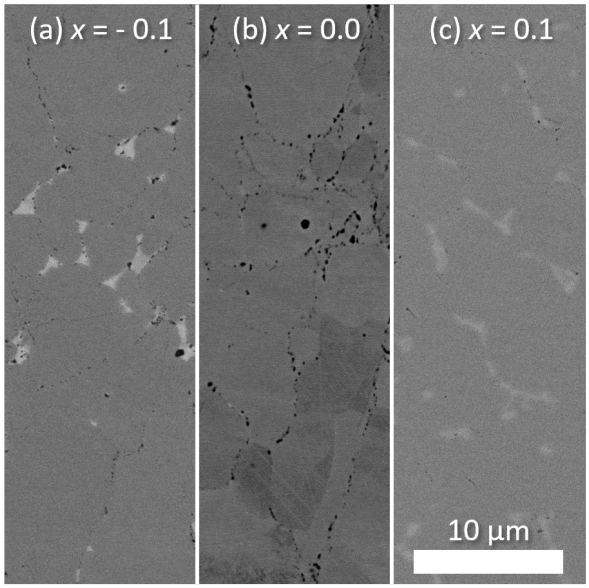

Figure 6. Scanning electron micrographs acquired with backscattered electrons (BSE) of $Ti_{1+x}Fe_{2-x}Sn$ for $x = -0.10$, 0.00, 0.10, in frames (a), (b) and (c), respectively, showing Z contrast between matrix and impurity phases. EDX identified the matrix phase as (a) Fe–rich or (c) Ti–rich, corresponding to the expected Ti:Fe ratio.

analysis. As the Fe–rich sample has an Fe–Sn impurity and the Ti–rich sample has a Ti–Sn impurity, these impurity phases are consistent with the experimental Ti:Fe ratio.

Physical Properties

To characterize the thermoelectric performance of these materials, high temperature physical property measurements, including Seebeck coefficient (S) and electrical resistivity (ρ), were carried out. Results for $Ti_{1+x}Fe_{2-x}Sn$ ($x = -0.10$, -0.05 0.00, 0.05, 0.10) are presented in Figure 7, and results for $TiFe_2Sn_{1-y}Sb_y$ ($y = 0.01$, 0.05) are illustrated in Figure 8.

Panel (a) of Figure 7 exhibits trends in electrical resistivity with x as a function of temperature showing that resistivity has limited dependence on shifts in composition. Room temperature resistivity values are similar to those published elsewhere,[26] and an increase in resistivity for $x = 0.10$, shown here, has also been observed elsewhere.[22] All of the samples display electrical resistivity values that are significantly smaller than the Mott maximum metallic resistivity value close to $10^{-2}\,\Omega\,$cm that would be expected of semiconducting samples. In other words, all the samples behave like metals, despite the expectation of a band gap as suggested by the DFT calculations. The rather flat temperature-dependence of the electrical resistivity of all the compounds is characteristic of so-called "dirty" metals, similar to what has been seen in the Heusler compound VFe_2Al,[12, 13, 14] other Heusler-dervived materials[39] and disordered metals.[40, 41] Similar behavior has been observed in lower-temperature measurements on $TiFe_2Sn$ Heusler compounds.[22, 23] Electronic

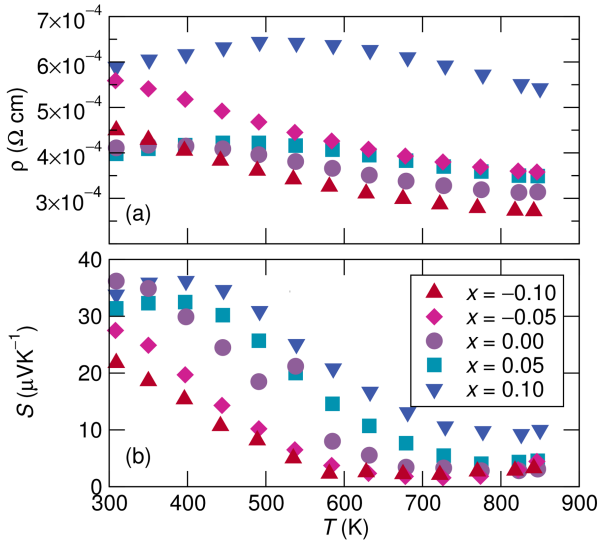

Figure 7. (a) Electrical resistivity (ρ) of the $Ti_{1+x}Fe_{2-x}Sn$ series indicates small increases in resistivity with x with relatively flat temperature dependence, while the (b) Seebeck coefficient is decreased for Fe–rich samples.

structure calculations of disordered $TiFe_2Sn$ suggest that introduction of anti-site defects introduces associated states at the Fermi level. [26]

Panel (b) of Figure 7 illustrates the dependence of the Seebeck coefficient with respect to temperature for the $Ti_{1+x}Fe_{2-x}Sn$ material. The Seebeck coefficient is reduced in Fe–rich samples and remains constant for Ti–rich samples, although the temperature of the Seebeck coefficient peak does transition to higher temperature with increasing x into Ti–rich compositions. These results are consistent with low temperature studies.[23, 22] The Seebeck coefficient is consistently positive, revealing that holes are the dominant carrier for all $TiFe_2Sn$ samples. These results separate $TiFe_2Sn$ from Heusler compound VFe_2Al, which has a Seebeck coefficient that is highly sensitive to atomic ratio: pure VFe_2Al has a maximum Seebeck coefficient near $30\,\mu VK^{-1}$, and variations in stoichiometry, such as varying the V:Al[18] or V:Fe[17] ratio, or doping the Al site with Ge[15] can enhance it to $80\,\mu VK^{-1}$ or $-120\,\mu VK^{-1}$.

Figure 8 illustrates the effects on thermoelectric properties resulting from the substitution of Sn for Sb in the form $TiFe_2Sn_{1-y}Sb_y$ ($y = 0.01$, 0.05). Sb is expected to act as an electron donor and, through the introduction of electrons, a large n-type Seebeck coefficient has been predicted for $TiFe_2Sn$.[11] Electrical resistivity results, displayed in panel (a), show that the $y = 0.01$ is more resistive than the stoichiometric compound, while at $y = 0.05$ resistivity returns to near that of the stoichiometric compound. However, all values remain within the same order of magnitude, suggesting no considerable impact on electrical resistivity. In contrast to variations in the resistivity with changes to the Ti:Fe ratio, the slope of resistivity remains unchanged with y. Panel (b) of Figure 8 illustrates that the Seebeck coefficient is reduced through the introduction of Sb, due to the compensation on intrinsic holes

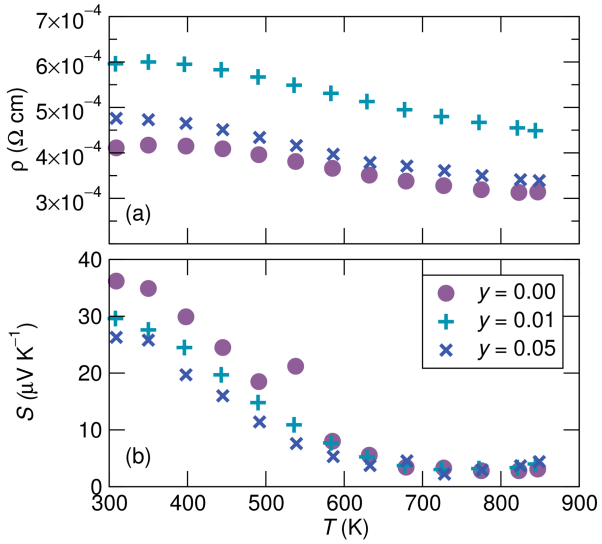

Figure 8. (a) Electrical resistivity of the $TiFe_2Sn_{1-y}Sb_y$ series indicates that resistivity is increased upon the introduction of Sb, while (b) the Seebeck coefficient decreases upon Sb introduction.

by the doped electrons, but that the Seebeck coefficient does not change sign and display n-type behavior. These results are in contrast to VFe_2Al, which starts off as n-type, and further electron doping results in a reduction in electrical resistivity and Seebeck coefficient enhancement to $-120\,\mu VK^{-1}$ upon the substitution of either Si[15] or Ge for Al.[16] As highlighted in our structural analysis, $TiFe_2Sn$ contains Ti/Fe anti-site disorder that have been shown elsewhere[26] to known to modify the band structure from what is calculated assuming a fully ordered, defect free material. In the defective electronic structure, excess Sb electrons compensate the intrinsic holes, and are detrimental to the transport properties.

Conclusions

Derivatives of the Heusler compound $TiFe_2Sn$ were studied via synchrotron X-ray and neutron diffraction, electron microscopy, and thermoelectric physical property measurements (Seebeck coefficient and electrical resistivity). A series of compounds with varied Ti:Fe ratio ($Ti_{1+x}Fe_{2-x}Sn$, $x = -0.10$, -0.05 0.00, 0.05, 0.10) were studied. The closest-to-stoichiometry compound exhibits approximately 5% Ti:Fe anti-site disorder, and the degree of disorder is decreased for Ti–rich starting compositions. Studies considering Sb doping ($TiFe_2Sn_{1-y}Sb_y$, $y = 0.01$, 0.05) show that Sb doping does not significantly enhance the Seebeck coefficient because the doped electrons primarily serve to compensate the intrinsically p-type material.

Acknowledgments

This work was supported by the MRSEC Program of the National Science Foundation through DMR 1121053. M.L.C.B. is supported by the National Science Foundation Graduate Research Fellowship Program under Grant No. 1144085. The Materials Research Laboratory is a member of the NSF-supported Materials Research Facilities Network. Use of the Advanced Photon Source at Argonne National Laboratory was supported by the U. S. Department of Energy, Office of Science, Office of Basic Energy Sciences, under Contract No. DE-AC02-06CH11357. Neutron data collection used the POWGEN mail-in service at the Oak Ridge National Laboratory Spallation Neutron Source, sponsored by the Scientific User Facilities Division, Office of Basic Energy Sciences, US Department of Energy.

[1] G. J. Snyder and E. S. Toberer. Complex thermoelectric materials. *Nat. Mater.*, 7:105, 2008.

[2] X. Yan, B. Poudel, Y. Ma, W. Liu, G. Joshi, H. Wang, Y. Lan, D. Wang, G. Chen, and Z. Ren. Experimental studies on anisotropic thermoelectric properties and structures of n-type $Bi_2Te_{2.7}Se_{0.3}$. *Annalen der Physik*, 10:3373, 2010.

[3] H. Kleinke. New bulk materials for thermoelectric power generation: Clathrates and complex antimonides. *Chem. Mater.*, 22:604, 2010.

[4] X. Shi, J. Yang, J. Salvador, M. Chi, J. Cho, H. Wang, S. Bai, J. Yang, W. Zhang, and L. Chen. Multiple-filled skutterudites: High thermoelectric figure of merit through separately optimizing electrical and thermal transports. *J. Am. Chem. Soc.*, 133:7837, 2011.

[5] S. Chen and Z. Ren. Recent progress of half-Heusler for moderate temperature thermoelectric applications. *Mater. Today*, 16:287, 2013.

[6] F. Heusler. Manganese bronze and synthesis of magnetizable alloys from nonmagnetic metals. *Angew. Chem*, 17:260, 1904.

[7] T. Graf, C. Felser, and S. Parkin. Simple rules for the understanding of Heusler compounds. *Prog. Solid State Chem.*, 39:1, 2011.

[8] M. L. C. Buffon, G. Laurita, N. Verma, L. Lamontagne, L. Ghadbeigi, D. L. Lloyd, T. D. Sparks, T. M. Pollock, and R. Seshadri. Enhancement of thermoelectric properties in the NbCoSn half-Heusler/Heusler system through spontaneous inclusion of a coherent second phase. *J. Appl. Phys*, 120:075104, 2016.

[9] J. E. Douglas, P. A. Chater, C. M. Brown, T. M. Pollock, and R. Seshadri. Nanoscale structural heterogeneity in Ni-rich half-Heusler TiNiSn. *J. Appl. Phys.*, 116:163514, 2014.

[10] P. Qiu, J. Yang, X. Huang, X. Chen, and L. Chen. Effect of antisite defects on band structure and thermoelectric performance of ZrNiSn half-Heusler alloys. *Appl. Phys. Lett*, 96:152105, 2010.

[11] S. Yabuuchi, M. Okamoto, A. Nishide, Y. Kurosaki, and J. Hayakawa. Large Seebeck coefficients of Fe_2TiSn and Fe_2TiSi: First-principles study. *Appl. Phys. Express*, 6:025504, 2013.

[12] Y. Nishino, M. Kato, S. Asano, K. Soda, M. Hayasaki, and U. Mizutani. Semiconductorlike behavior of electrical resistivity in Heusler-type Fe_2VAl compound. *Phys. Rev. Lett.*, 79:1909, 1997.

[13] R. Weht and W. E. Pickett. Excitonic correlations in the intermetallic Fe_2VAl. *Phys. Rev. B*, 58:6855, 1998.

[14] D. J. Singh and I. I. Mazin. Electronic structure, local moments, and transport in Fe_2VAl. *Phys. Rev. B*, 57:14352, 1998.

[15] Y. Nishino, S. Deguchi, and U. Mizutani. Thermal and transport properties of the Heusler-type $Fe_2VAl_{1-x}Ge_x (0 \leq x \leq 0.20)$ alloys: Effect of doping on lattice thermal conductivity, electrical

resistivity, and Seebeck coefficient. *Phys. Rev. B*, 74:115115, 2006.
[16] C. S. Lue, C. F. Chen, J. Y. Lin, Y. T. Yu, and Y. K. Kuo. Thermoelectric properties of quaternary Heusler alloys $Fe_2VAl_{1-x}Si_x$. *Phys. Rev. B*, 75:064204, 2007.
[17] T. Kanomata, T. Sasaki, T. Hoshi, T. Narita, T. Harada, H. Nishihara, T. Yoshida, R. Note, K. Koyama, H. Nojiri, T. Kaneko, and M. Motokawa. Magnetic and electrical properties of $Fe_{2+x}V_{1-x}Al$. *J. Alloys Compd.*, 317-318:390, 2001.
[18] H. Miyazaki, S. Tanaka, N. Ide, K. Soda, and Y. Nishino. Thermoelectric properties of Heusler-type off-stoichiometric $Fe_2V_{1+x}Al_{1-x}$ alloys. *Materials Research Express*, 1:015901, 2014.
[19] M. Mikami, M. Inukai, H. Miyazaki, and Y. Nishino. Effect of off-stoichiometry on the thermoelectric properties of Heusler-type Fe_2VAl sintered alloys. *J. Electron Mater.*, 45:1284, 2016.
[20] C. S. Lue and Y.-K. Kuo. Thermoelectric properties of the semimetallic Heusler compounds $Fe_{2-x}V_{1+x}M$ (M = Al, Ga). *Phys. Rev. B.*, 66:085121, 2002.
[21] T. Nakama, Y. Takaesu, K. Yagasaki, T. Naka, A. Matsushita, K. Fukuda, and Y. Yamada. Transport properties of Heusler compounds $Fe_{3-x}V_xAl$. *J. Phys. Soc. Jpn.*, 74:1378, 2005.
[22] C. S. Lue and Y.-K Kuo. Thermal and transport properties of the Heusler-type compounds $Fe_{2-x}Ti_{1+x}Sn$. *J. Appl. Phys.*, 96:2681, 2004.
[23] M. Nakabayashi, K. Fukuda, H. Kitagawa, Y. Yamada, S. Kubo, and A. Matsushita. Magnetic and transport properties in Heusler-type Fe_2TiSn compound. *Physica B*, 329-333:1134, 2003.
[24] A. Slebarski, M. B. Maple, C. Sirvent E. J. Freeman, D. Tworuszka, M. Orzechowska, A. Wrona, A. Jezierski, S. Chiuzbaian, and M. Neumann. Weak ferromagnetism induced by atomic disorder in Fe_2TiSn. *Phys. Rev. B*, 62:3296, 2000.
[25] J. E. Frackowiak and J. Deniszczyk. Mossbauer effect study of atomic disorder in Fe_2TiSn alloy. *Mol. Phys. Rep.*, 38:79, 2003.
[26] A. Slebarski. Electron-correlation effects in a disordered Fe_2TiSn Heusler alloy. *J. Phys. D: Appl. Phys.*, 39:856, 2006.
[27] G. Kresse and J. Fürthmuller. Efficiency of ab-initio total energy calculations for metals and semiconductors using a plane-wave basis set. *Comput. Mater. Sci.*, 6:15, 1996.
[28] G. Kresse, M. Marsman, J. Fürthmuller, and J. Vienna. Ab-initio simulation package: VASP the guide. , 2012.
[29] P. E. Blöchl. Projector augmented-wave method. *Phys. Rev. B*, 50:17953, 1994.
[30] G. Kresse and D. Joubert. From ultrasoft pseudopotentials to the projector augmented-wave method. *Phys. Rev. B*, 59:1758, 1999.
[31] J. Perdew, K. Burke, and M. Ernzerhof. Generalized gradient approximation made simple. *Phys. Rev. Lett.*, 77:3865, 1996.
[32] A. Coelho. Topas academic v5 software. http://www.topas-academic.net/, 2012.
[33] K. Momma and F. Izumi. VESTA3 for three-dimensional visualization of crystal, volumetric and morphology data. *J. Appl. Cryst*, 44:1272, 2011.
[34] J. Jong, J. Zhu, M.-G. Jon, Y. Zhou, J. Kim, and J. Yan. Theoretical investigation of stabilities and physical properties of low cost Fe-based full-Heusler materials. *J. Alloys Compd.*, 693:462, 2017.
[35] H. Luo, G. Liu, F Meng, J. Li, E. Liu, and G Wu. Half-metallicity in Fe-based Heusler alloys Fe_2TiZ (Z = Ga, Ge, As, In, Sn and Sb). *J. Magn. Magn. Mater.*, 324:3295, 2012.
[36] B. Xu and L. Yi. Optical properties of the intermetallic compound Fe_2TiSn. *J. Phys. D: Appl. Phys.*, 41:095404, 2008.
[37] V. F. Sears. Neutron scattering lengths and cross sections. *Neutron News*, 3:26–37, 1992.
[38] A. Denton and N. Ashcroft. Vegard's law. *Phys. Rev. A*, 43:3161, 1991.
[39] L. Jodi, J. Tobola, P. Pecheur, H. Scherrer, and S. Kaprzyk. Effect of substitutions and defects in half-Heusler FeVSb studied by electron transport measurements and KKR-CPA electronic structure calculations. *Phys. Rev. B*, 70:184207, 2004.
[40] P.J. Cote. Electrical resistivity of amorphous nickel phosphorus alloys. *Solid State Commun.*,

18:1311, 1976.

[41] M. Kass, C. Brooks, D. Falcon, and D. Basak. Electrical resistivity of amorphous nickel phosphorus alloys. *Intermetallics*, 10:951, 2002.